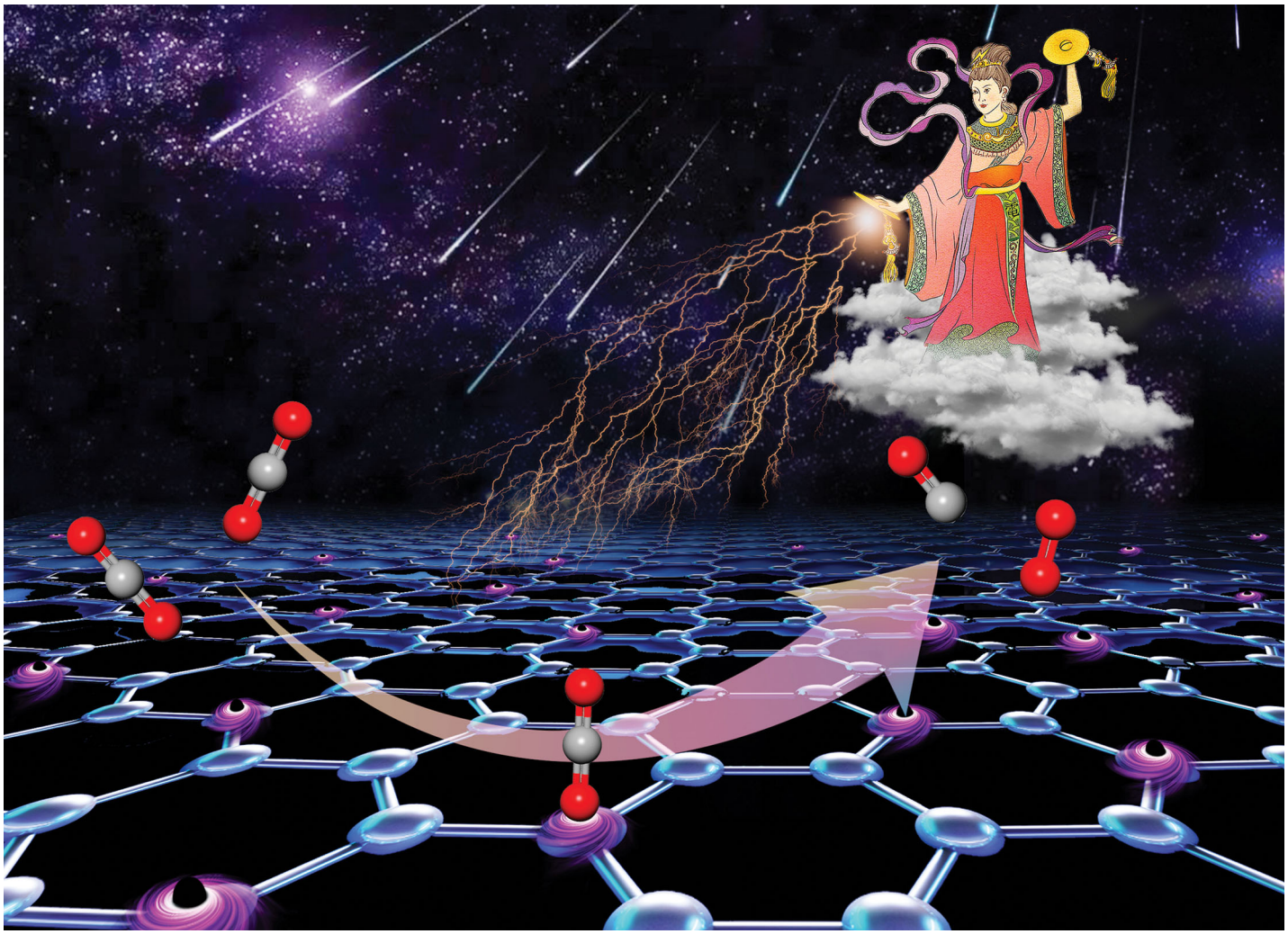

**Showcasing research from Professor Li Wang's group at Dalian Maritime University, China and Professor Xin Tu's group at the University of Liverpool, UK**

Plasma-enhanced direct conversion of $CO_2$ to CO over oxygen-deficient Mo-doped $CeO_2$

Plasma-catalytic direct splitting of $CO_2$ to CO over oxygen-deficient Mo-doped $CeO_2$ at ambient conditions was achieved. Developing new catalytic technologies involving plasma opens the door to unlocking the potential of using captured $CO_2$ to make valuable chemicals under mild conditions.

## As featured in:

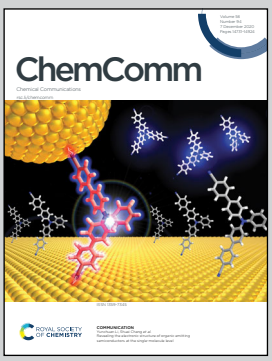


See Li Wang, Xin Tu *et al.*, *Chem. Commun.*, 2020, **56**, 14801.

ROYAL SOCIETY OF CHEMISTRY

rsc.li/chemcomm

Registered charity number: 207890

ChemComm

COMMUNICATION

View Article Online
View Journal | View Issue



Cite this: *Chem. Commun.*, 2020, **56**, 14801

Received 28th September 2020,
Accepted 6th November 2020

DOI: 10.1039/d0cc06514e

rsc.li/chemcomm



# Plasma-enhanced direct conversion of $CO_2$ to CO over oxygen-deficient Mo-doped $CeO_2$†

Li Wang, *[a] Xiaomin Du,[a] Yanhui Yi,[b] Hongyang Wang,[a] Masaud Gul,[a] Yimin Zhu[a] and Xin Tu *[c]

**Plasma $CO_2$ splitting to CO over oxygen-deficient Mo-doped $CeO_2$ under mild conditions was investigated for the first time, showing ~20 times higher $CO_2$ conversion compared to pure $CeO_2$, which can be attributed to the increased oxygen vacancies ($V_O$) and the formation of $Ce^{3+}$–$V_O$–Mo on the catalyst surface. Importantly, $V_O$ sites showed excellent catalytic stability.**

Converting $CO_2$ to value-added fuels and chemicals has been considered as a promising route in $CO_2$ utilization. Significant efforts have been devoted to the chemical transformation of $CO_2$, including thermal catalysis,[1] photocatalysis,[2,3] electrocatalysis,[4,5] and plasma catalysis.[6,7] Direct splitting of $CO_2$ to CO without using any reductant is attractive for $CO_2$ conversion, as CO is an important chemical feedstock for the synthesis of a range of chemicals and fuels. However, this reaction has to overcome a strong thermodynamic barrier ($CO_2 \rightarrow CO + 1/2O_2$, $\Delta H_{298K}$ = 280 kJ $mol^{-1}$ = 2.9 eV $molecule^{-1}$) to break the C=O bond, since $CO_2$ is very stable. Ultrahigh temperatures (2000 K) are often required to activate $CO_2$ (Fig. S1, ESI†).

In recent years, using non-thermal plasmas (NTPs) for the activation of inert molecules with strong chemical bonds (*e.g.*, $CO_2$, $CH_4$ and $N_2$) under mild conditions has attracted significant interest, including $CO_2$ reforming with $CH_4$ to oxygenates,[8,9] $CO_2$ hydrogenation to methanol,[10] and ammonia synthesis.[11] NTP is rich in energetic electrons with a typical energy of 1–10 eV, which is sufficient to activate reactants into chemically reactive species, enabling thermodynamically unfavorable reactions (*e.g.* $CO_2$ splitting) to proceed at ambient conditions.

Up until now, studies on plasma $CO_2$ splitting to CO mainly focused on the optimization of operating parameters,[12–16] and only a few catalysts (*e.g.*, $Ni/SiO_2$, $NiO/TiO_2$ and $Rh/TiO_2$) have been evaluated (Table S1, ESI†).[17–20] Recently, surface oxygen vacancies ($V_O$) have been suggested to be the active sites in plasma-catalytic $CO_2$ splitting to CO. Mei *et al.* reported that higher $CO_2$ conversion was achieved when coupling plasma with $BaTiO_3$, which can be explained by the formation of more $V_O$ sites on the surfaces of $BaTiO_3$ compared with $TiO_2$.[20] Chen *et al.* found the $V_O$ on $Ni/TiO_2$ contributed to the enhanced $CO_2$ dissociation.[18] In fact, the coupling of catalysts and plasma is a promising strategy to improve $CO_2$ conversion and energy efficiency. However, the knowledge in selection of appropriate catalysts for highly efficient $CO_2$ splitting to CO using NTP was still very limited until now.

Herein, $CO_2$ splitting to CO over M-doped $CeO_2$ catalysts (M = Fe, Co, Ni, Cu, Cr, V, Mn or Mo) has been carried out in a dielectric barrier discharge (DBD) reactor (Fig. S2–S5, ESI†). $CeO_2$ not only serves as a support to anchor and disperse the metal oxide particles but also generates $V_O$ active sites through the interaction with metal oxides. Significant differences were observed among the M-doped $CeO_2$ catalysts in terms of $CO_2$ conversion, and the Mo-doped $CeO_2$ exhibited the best activity in $CO_2$ conversion (Fig. S3, ESI†). Therefore, Mo-doped $CeO_2$ has been selected for further studies.

Comprehensive catalyst characterization was carried out to understand the physicochemical properties of Mo-doped $CeO_2$. As shown in Fig. 1, the X-ray diffraction (XRD) pattern of $CeO_2$ exhibits characteristic peaks of a cubic fluorite phase (JCPDS, 34-0394). For Mo-doped $CeO_2$, small peaks of α-$MoO_3$ (JCPDS, 05-0508) and $Mo_4O_{11}$ (JCPDS, 05-0337) are observed, revealing the coexistence of Mo(VI) and Mo(V) species. Notably, the characteristic peaks of $CeO_2$ downshift compared to pure $CeO_2$, which suggests that Mo doping leads to the expansion of the $CeO_2$ unit cell. Usually, inserting Mo ions into $CeO_2$ induces shrinkage of the $CeO_2$ unit cell since the radius of Mo ions is much smaller than that of Ce ions, resulting in upshifting of $CeO_2$ peaks, rather than downshifting. Thus, Mo ions do not insert into the $CeO_2$ unit cell, and there might be other reasons responsible for this downshift. X-ray photoelectron spectroscopy

[a] *College of Environmental Sciences and Engineering, Dalian Maritime University, Dalian, 116026, P. R. China. E-mail: liwang@dlmu.edu.cn*
[b] *State Key Laboratory of Fine Chemicals, School of Chemical Engineering, Dalian University of Technology, Dalian 116012, P. R. China*
[c] *Department of Electrical Engineering and Electronics, University of Liverpool, Liverpool, L69 3GJ, UK. E-mail: xin.tu@liv.ac.uk*

† Electronic supplementary information (ESI) available. See DOI: 10.1039/d0cc06514e

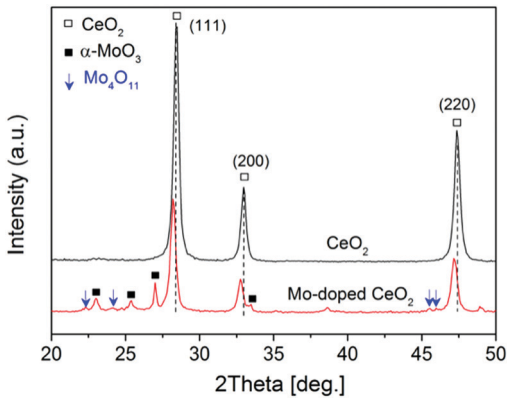


Fig. 1 XRD patterns of $CeO_2$ and as-prepared Mo-doped $CeO_2$.

(XPS) was employed to analyze surface properties of Mo-doped $CeO_2$. The deconvoluted Ce 3d XPS spectra are presented in Fig. 2(a). The peaks labeled as v, v′, v″′ and u, u″, u″′ are assigned to $3d_{5/2}$ and $3d_{3/2}$ electrons of $Ce^{4+}$, respectively, while the peaks of v′, u′ and $v_o$, $u_o$ correspond to $3d_{5/2}$ and $3d_{3/2}$ electrons of $Ce^{3+}$, respectively.[21] Clearly, $Ce^{3+}$ exists in $CeO_2$ and Mo-doped $CeO_2$, suggesting the formation of $V_O$ in both samples. More importantly, the proportion of $Ce^{3+}$ in Mo-doped $CeO_2$ is 40.2%, higher than that in $CeO_2$ (30.0%) (Fig. S6 and S7, ESI†). This finding suggests that Mo doping induces partial transformation of $Ce^{4+}$ to $Ce^{3+}$ and creates more $V_O$ on Mo-doped $CeO_2$. As reconfirmed by the O 1s XPS spectra in Fig. 2(b) and Fig. S6 (ESI†), a higher surface $V_O$ (30.4%) is achieved in the Mo-doped $CeO_2$ in comparison to pure $CeO_2$ (21.0%). Furthermore, the transformation of $Ce^{4+}$ to $Ce^{3+}$ leads to the expansion of the $CeO_2$ unit cell since the ion radius of $Ce^{3+}$ (1.23 Å) is higher than that of $Ce^{4+}$ (0.97 Å),[22] which explains the reason for the downshifting of $CeO_2$ peaks in Fig. 1. More interestingly, the binding energies of Ce 3d shift significantly towards higher values after Mo doping, revealing that the electron density of the surface $CeO_2$ species is lower in Mo-doped $CeO_2$ compared with pure $CeO_2$, which might be induced by the electron transfer from Ce to Mo, due to the higher electronegativity of Mo. These results suggest different properties of $V_O$ sites in the form of $Ce^{3+}$–$V_O$ in $CeO_2$ and $Ce^{3+}$–$V_O$–Mo in Mo-doped $CeO_2$, as well as the strong interaction between Mo and $CeO_2$, which agrees with the results of $H_2$-temperature programmed reduction ($H_2$-TPR), scanning electron microscopy (SEM) and transmission electron microscopy (TEM) (Fig. S8–S11, ESI†). Fig. 2(c) shows the deconvoluted Mo 3d spectra, in which the Mo-doped $CeO_2$ sample exhibits typical doublet peaks of $Mo^{6+}$ with an energy gap of *ca.* 3.1 eV, indicating the formation of $MoO_3$ in Mo-doped $CeO_2$.[23] The two smaller peaks observed, however, are identified to be $3d_{3/2}$ and $3d_{5/2}$ electrons of Mo(v), demonstrating the formation of the non-stoichiometric $MoO_{3-x}$,[23] which is consistent with the $Mo_4O_{11}$ species confirmed by the XRD analysis (Fig. 1). Fig. 2(d) shows the Raman spectra of $CeO_2$ and Mo-doped $CeO_2$. For pure $CeO_2$, the intense band at 465 $cm^{-1}$ is well-indexed to the typical F2g modes of a cubic $CeO_2$ fluorite structure, and the weak bands at 262, 597 and 1171 $cm^{-1}$ are assigned to $V_O$, reconfirming the XPS results in Fig. 2(a and b).[23] For Mo-doped $CeO_2$, the emerging Raman bands at 673, 824 and 997 $cm^{-1}$ are assigned to $MoO_3$ crystallites.[24] However, the band at 955 $cm^{-1}$ is associated with Mo suboxides ($MoO_{3-x}$).[24,25] These results indicate that the valence state of Mo in suboxides is $Mo^{5+}$. Moreover, the presence of $Mo^{5+}$ and $Ce^{3+}$ indicates that more $V_O$ sites are created through the strong interaction between Mo and $CeO_2$, as well as the calcining atmosphere with deficient oxygen and rich energetic Ar species, which agrees with the results reported by Chen *et al.*[18]

Fig. 3 shows the effect of different operating conditions on $CO_2$ conversion. Clearly, no reaction occurred without plasma (catalyst only, 400 °C). The conversion of $CO_2$ was 3.8% in the plasma reaction without a catalyst (plasma only). In the plasma reaction coupled with pure $CeO_2$, the $CO_2$ conversion dropped to 1.2%, which suggests that pure $CeO_2$ is unfavorable for $CO_2$ splitting to CO despite $CeO_2$ being O-deficient. Using Mo-doped

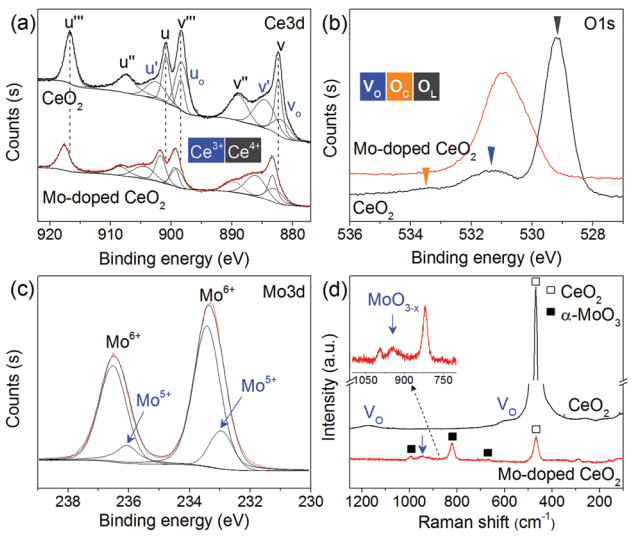


Fig. 2 XPS and Raman spectra of $CeO_2$ and as-prepared Mo-doped $CeO_2$ (a) Ce 3d, (b) O 1s, (c) Mo 3d and (d) Raman spectra ($V_O$, $O_C$ and $O_L$ represent oxygen vacancy, chemisorbed oxygen species and oxygen lattice, respectively).

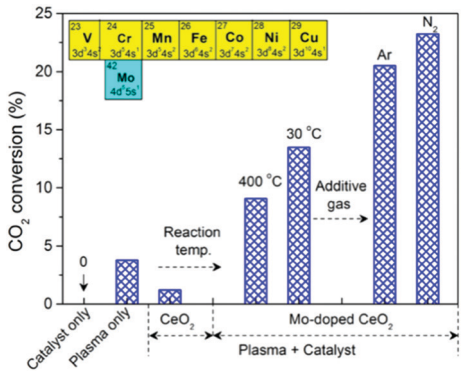


Fig. 3 Effect of reaction temperature and additive gas on $CO_2$ conversion ($CO_2$ flow rate 40 ml $min^{-1}$, SEI 20 kJ $L^{-1}$, molar ratio 4 : 1 and 30 °C for $CO_2$/Ar and $CO_2$/$N_2$; catalyst only 400 °C).

$CeO_2$ instead of $CeO_2$, however, results in a significant increase of $CO_2$ conversion by a factor of 9 at 400 °C. In addition, the Mo-doped $CeO_2$ showed stable $CO_2$ conversion for at least 10 h (Fig. S12, ESI†). Interestingly, the reaction performance can be further improved by using a lower reaction temperature (30 °C) and an additive gas (Ar or $N_2$). This promotional effect was more pronounced when adding $N_2$. The highest $CO_2$ conversion of 23.2% and energy efficiency of 14.3% were achieved in the plasma splitting of $CO_2$ with $N_2$ addition over Mo-doped $CeO_2$ at 30 °C (Table S1, ESI†), while the corresponding formation rate of CO and $O_2$ was 24.9 mmol $h^{-1}$ and 12.4 mmol $h^{-1}$, respectively (Table S2, ESI†). The optimal energy efficiency achieved in this study is comparable to that reported in previous works (Table S1, ESI†).

Regarding surface reactions, the improved activity over Mo-doped $CeO_2$, on one hand, is mainly attributed to the increased formation of $V_O$ (Fig. 2 and Fig. S6, ESI†), since $V_O$ serve as adsorption centers for $CO_2$ dissociative adsorption,[17,26] *i.e.*, $CO_2 + V_O \rightarrow O_L/O_C + CO$. On the other hand, the promoted performance originates from the different properties of $V_O$ in the forms of $Ce^{3+}$–$V_O$ and $Ce^{3+}$–$V_O$–Mo due to strong interaction between Mo and $CeO_2$ and the higher electronegativity of Mo compared with Ce (Fig. 1, 2 and Fig. S8, ESI†), which leads to a stronger binding strength of $CO_2$ with the $V_O$ of $Ce^{3+}$–$V_O$–Mo. As discussed above, $V_O$ is the active site for $CO_2$ activation; thus, the stability of $V_O$ greatly influences the subsequent catalytic cycle. It is well recognized that oxygen can be produced in plasma $CO_2$ splitting, and the produced O species could poison the catalyst through filling $V_O$ sites to form stable lattice oxygen species, resulting in termination of the catalytic cycle.

Therefore, the spent Mo-doped $CeO_2$ catalysts were further characterized by XPS, Raman, XRD and $H_2$-TPR (Fig. 4). Interestingly, compared with the fresh catalyst, the spent Mo-doped $CeO_2$ catalysts show an increased amount of $Ce^{3+}$ and $MoO_{3-x}$, which can be confirmed by the higher intensities of $Ce^{3+}$ peaks and the Raman band at ~950 $cm^{-1}$ in Fig. 4(a and b), respectively. The enhancement effect is more pronounced for the catalyst used at 400 °C. Correspondingly, more $V_O$ sites were created in the high-temperature reaction (Table S3, ESI†). In addition, the color of the catalyst changed from gray/blue ($MoO_{3-x}$) to yellow ($MoO_{3-y}$) with $x > y$ after the reaction at 30 °C, while no visible changes were observed on the phase structure of Mo-doped $CeO_2$ before and after the reaction (30 °C), as shown in Fig. 4(c). These results indicate that some O atoms from $CO_2$ splitting are adsorbed onto the catalyst, as seen by the slightly increased $H_2$ consumption in Fig. 4(d). Even so, the $V_O$ concentration of Mo-doped $CeO_2$ used at 30 °C remained at a similar level with that of the fresh sample (Table S3, ESI†). These findings suggest that $V_O$-rich Mo-doped $CeO_2$ is stable after the plasma reaction, and high-temperature reactions facilitate the formation and recovery of $V_O$ sites, resulting from accelerating recombinative desorption of adsorbed O atoms.[27]

In addition to surface reactions, gas-phase reactions also play a crucial role in the plasma-catalytic process. In a pure $CO_2$ DBD, $CO_2$ splitting to CO mainly proceeds through the electron impact dissociation of $CO_2$ ($CO_2 + e \rightarrow CO + O + e$), which can be confirmed by plasma chemical kinetic modeling,[28] as well as the formation of CO bands and O atomic lines detected by optical emission spectra of $CO_2$ DBD (Fig. 5(a)). As shown in Fig. 5(a), the presence of strong $N_2$ ($C^3\Pi_u \rightarrow B^3\Pi_g$, $B^3\Pi_g \rightarrow A^3\Sigma_u^+$) molecular bands and Ar atomic lines suggests the formation of excited nitrogen species ($N_2$*) and metastable Ar species (Ar*).[29,30] These species create an additional reaction route for $CO_2$ dissociation ($N_2$* (or Ar*) + $CO_2 \rightarrow CO + O + N_2$ (or Ar)), supported by the increased intensity of O atomic lines and CO bands when adding $N_2$ or Ar, which contributes to the enhanced $CO_2$ conversion. Furthermore, 150 ppm $NO_x$ was detected by Fourier transform infrared (FTIR) in the case of $N_2$ addition (Fig. S13, ESI†), revealing that $N_2$ can be regarded as an alternative scavenger of O species.[12] The elimination of partial O species can effectively limit the reverse reaction, *i.e.*, $O + CO + M \rightarrow CO_2 + M$, and thus enhance the $CO_2$ conversion. This could explain why adding $N_2$ has a stronger promotion on the $CO_2$ conversion compared with Ar.

Interaction between reactive species in the gas phase and catalyst is also crucial in plasma-catalytic reactions.[31] Compared to plasma only, packing Mo-doped $CeO_2$ into the

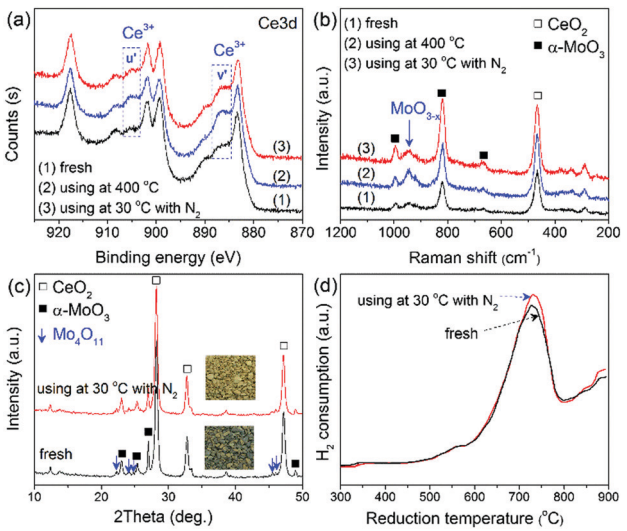


Fig. 4 (a) XPS spectra, (b) Raman spectra, (c) XRD patterns, (d) $H_2$-TPR profiles of Mo-doped $CeO_2$ before and after reaction.

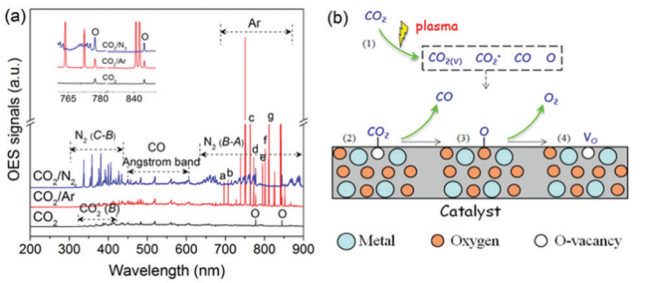


Fig. 5 (a) Emission spectra of $CO_2$ plasma, (b) possible pathways of plasma-catalytic $CO_2$ splitting over $V_O$-rich catalyst.

discharge zone decreased the current (Fig. S14, ESI†), lowering the contribution of the gas-phase reactions. In this case, the $CO_2$ conversion, however, was still improved, which might be attributed to the interaction between active species and $V_O$-rich Mo-doped $CeO_2$, accelerating $V_O$ recovery. Therefore, a possible reaction mechanism is proposed in Fig. 5(b). Firstly, $CO_2$ is activated to species of $CO_2^+$, $CO_{2(v)}$, CO and O radicals as shown in Fig. 5(a) (step 1). Then, the energetic $CO_2$-species are adsorbed on the $V_O$ sites to decrease their internal energy (step 2). After that, the $V_O$ sites have the potential to grasp the O atom of the adsorbed $CO_2$ molecule, which weakens the C═O bond, producing adsorbed CO and O (step 3). Subsequently, the adsorbed CO desorbs as the final CO product. While the adsorbed O mainly desorbs from $V_O$ sites in the form of $O_2$ through reacting with the active O radicals produced in the gas phase ($O_g + O_{ad}–V_O \rightarrow O_{2,g} + V_O$), *i.e.*, Eley–Rideal (E–R) mechanism. Meanwhile, $V_O$ sites recover completing the catalytic cycle (step 4). Using isotope trace analysis, we demonstrated the desorption of $N_{ad}$ through an E–R reaction in plasma-catalytic $NH_3$ decomposition.[31] Therefore, the desorption of $O_{ad}$ through E–R reaction is also expected. Note that, too strong of a $CO_2$–$V_O$ bond makes it easy to split the $CO_2$ molecule, but the corresponding desorption of adsorbed O is difficult. By contrast, too weak of a $CO_2$–$V_O$ bond means it could be hard to split $CO_2$, although the adsorbed O can easily desorb from the catalyst surface. Therefore, a catalyst with a proper binding strength between $V_O$ sites and $CO_2$ benefits the conversion of $CO_2$ and favors the catalytic cycle.

In conclusion, plasma-catalytic $CO_2$ splitting over M-doped $CeO_2$ catalysts (M = Fe, Co, Ni, Cu, Cr, V, Mn or Mo) has been investigated. Mo-doped $CeO_2$ exhibited the best activity; this is attributed to the increased oxygen vacancies created by strong interaction between Mo and $CeO_2$, as well as the calcining atmosphere being oxygen-deficient and rich in Ar metastable species. Furthermore, oxygen vacancies were stable during the reaction, which is ascribed to the interaction between active O produced in the gas phase and the adsorbed O on the oxygen vacancy site, resulting in desorbing as $O_2$ molecules and recovering oxygen vacancy sites. These findings suggest that introducing proper doping on $CeO_2$ offers a potential route to tune properties of oxygen vacancy in $CeO_2$. Additionally, adding $N_2$ and Ar into the plasma process enhanced the $CO_2$ conversion, especially when adding $N_2$. This promotional effect is mainly attributed to the new reaction routes induced by the presence of metastable species. We found that $N_2$ can be used as an O scavenger to forward the chemical equilibrium and inhibit the reverse reaction to form $CO_2$.

This work was financially supported by the NSFC (No. 21908016), the Liaoning Natural Science Foundation (No. 2019-MS-023 and 2018011143-301), the key Science and Technology Project List of Ministry of Transport of the People's Republic of China (No. 2018-ZD4-027). X. Tu acknowledges the funding from the European Union's Horizon 2020 research and innovation programme under the Marie Sklodowska-Curie grant agreement no. 823745 and the State Key Laboratory of Electrical Insulation and Power Equipment at Xi'an Jiaotong University (No. EIPE19207), China.

## Conflicts of interest

There are no conflicts to declare.

## Notes and references

1 J. Zhong, X. Yang, Z. Wu, B. Liang, Y. Huang and T. Zhang, *Chem. Soc. Rev.*, 2020, **49**, 1385.
2 S. Xie, Q. Zhang, G. Liu and Y. Wang, *Chem. Commun.*, 2016, **52**, 35.
3 Y. Lan, Y. Xie, J. Chen, Z. Hu and D. Cui, *Chem. Commun.*, 2019, **55**, 8068.
4 D. U. Nielsen, X. Hu, K. Daasbjerg and T. Skrydstrup, *Nat. Catal.*, 2018, **1**, 244.
5 X. Yuan, Y. Luo, B. Zhang, C. Dong, J. Lei, F. Yi, T. Duan, W. Zhu and R. He, *Chem. Commun.*, 2020, **56**, 4212.
6 A. George, B. Shen, M. Craven, Y. Wang, D. Kang, C. Wu and X. Tu, *Renewable Sustainable Energy Rev.*, 2021, **135**, 109702.
7 A. Bogaerts, X. Tu, J. C. Whitehead, G. Centi, L. Lefferts, O. Guaitella, F. A. Jury, H. H. Kim, A. B. Murphy, W. F. Schneider, T. Nozaki, J. C. Hicks, A. Rousseau, F. Thevenet, A. Khacef and M. Carreon, *J. Phys. D: Appl. Phys.*, 2020, **53**, 443001.
8 D. Li, V. Rohani, F. Fabry, A. P. Ramaswamy, M. Sennour and L. Fulcheri, *Appl. Catal., B*, 2020, **261**, 118228.
9 L. Wang, Y. Yi, C. Wu, H. Guo and X. Tu, *Angew. Chem., Int. Ed.*, 2017, **56**, 13679.
10 L. Wang, Y. Yi, H. Guo and X. Tu, *ACS Catal.*, 2018, **8**, 90.
11 Y. Wang, M. Craven, X. Yu, J. Ding, P. Bryant, J. Huang and X. Tu, *ACS Catal.*, 2019, **9**, 10780.
12 R. Snoeckx, S. Heijkers, K. V. Wesenbeeck, S. Lenaerts and A. Bogaerts, *Energy Environ. Sci.*, 2016, **9**, 999.
13 D. Mei and X. Tu, *J. $CO_2$ Util.*, 2017, **19**, 68.
14 D. Mei, X. Zhu, Y. He, J. D. Yan and X. Tu, *Plasma Sources Sci. Technol.*, 2015, **24**, 015011.
15 K. V. Laer and A. Bogaerts, *Plasma Processes Polym.*, 2017, **14**, 1600129.
16 D. Ray and C. Subrahmanyam, *RSC Adv.*, 2016, **6**, 39492.
17 K. Zhang, G. Zhang, X. Liu, A. N. Phan and K. Luo, *Ind. Eng. Chem. Res.*, 2017, **56**, 3204.
18 G. Chen, V. Georgieva, T. Godfroid, R. Snyders and M. Delplancke-Ogletree, *Appl. Catal., B*, 2016, **190**, 115.
19 L. F. Spencer and A. D. Gallimore, *Plasma Sources Sci. Technol.*, 2013, **22**, 015019.
20 D. Mei, X. Zhu, C. Wu, B. Ashford, P. T. William and X. Tu, *Appl. Catal., B*, 2016, **182**, 525.
21 C. Anandan and P. Bera, *Appl. Surf. Sci.*, 2013, **283**, 297.
22 W. Wang, Q. Zhu, F. Qin, Q. Dai and X. Wang, *Chem. Eng. J.*, 2018, **333**, 226.
23 K. Murugappan, E. M. Anderson, D. Teschner, T. E. Jones, K. Skorupska and Y. Román-Leshkov, *Nat. Catal.*, 2018, **1**, 960.
24 B. Liu, L. France, C. Wu, Z. Jiang, V. L. Kuznetsov, H. A. Al-Megren, M. Al-Kinany, S. A. Aldrees, T. Xiao and P. P. Edwards, *Chem. Sci.*, 2015, **6**, 5152.
25 K. Chen, S. Xie, A. T. Bell and E. Iglesia, *J. Catal.*, 2001, **198**, 232.
26 L. Liang, X. Li, Y. Sun, Y. Tan, X. Jiao, H. Ju, Z. Qi, J. Zhu and Y. Xie, *Joule*, 2018, **2**, 1004.
27 P. G. Dickens and M. B. Sutcliffe, *Trans. Faraday Soc.*, 1964, **60**, 1272.
28 R. Aerts, T. Martens and A. Bogaerts, *J. Phys. Chem. C*, 2012, **116**, 23257.
29 Y. Horikawa, T. Hayashi and K. Sasaki, *Jpn. J. Appl. Phys.*, 2012, **51**, 126301.
30 J. B. Boffard, G. A. Piech, M. F. Gehrke, L. W. Anderson and C. C. Lin, *Phys. Rev. A: At., Mol., Opt. Phys.*, 1999, **59**, 2749.
31 L. Wang, Y. Zhao, C. Y. Liu, W. M. Gong and H. C. Guo, *Chem. Commun.*, 2013, **49**, 3787.

 